Magneto-Optical Trap with Millimeter Ball Lenses

Cainan S. Nichols[1], Leo M. Nofs[1,2,‡] Michael A. Viray[2,*] Lu Ma,[2] Eric Paradis[1,†] and
Georg Raithel[2]

[1]*Department of Physics and Astronomy, Eastern Michigan University, Ypsilanti, Michigan 48197, USA*
[2]*Department of Physics, University of Michigan, Ann Arbor, Michigan 48109, USA*

We present a magneto-optical trap (MOT) design based on millimeter ball lenses, contained within a metal cube of 19-mm side length. The ball lenses create highly divergent conical MOT trapping beams. In our experiment and in trajectory simulations, we study the effect of beam divergence and light-intensity gradients on MOT performance. We trap approximately 4.2×10^5 ^{85}Rb atoms in our ball-lens MOT at a density of 3.2×10^9 cm^{-3} and a loading time of 1.3 s. Experimental measurements and the trajectory model are used to calibrate the trapping efficiency in the highly divergent light fields of the ball lenses. The advantages of the design include small lens and chamber sizes favorable to miniaturization, the absence of large-diameter optical-beam pathways, and a low laser-power requirement. These features are conducive to atom-trap geometries with well-defined electromagnetic boundary conditions, as required for ion and plasma traps, and for efficient shielding of black-body and dc stray fields.

I. INTRODUCTION

The invention of the magneto-optical trap (MOT) [1–3] has brought forth a variety of innovations in physics research, as it has allowed researchers to cool atoms to previously unattainable temperatures. Multiple groups have created MOT designs that use the same tangible principles but feature different optical configurations, often for the sake of miniaturization, portability, and/or ease of setup. These include grating MOTs [4,5], pyramidal MOTs [6–9], low-velocity intense-source (LVIS) MOTs [10], and five-beam MOTs [11]. While implementations of the classic six-beam MOT design suffice for many cold-atom experiments, some applications require electromagnetic boundary conditions that are better defined than what is afforded by the broadly optically accessible structure of a standard MOT.

Here, we realize a MOT design that uses millimeter-sized ball lenses that are held in place in a cubic metal frame with a side length of 19 mm, contained inside a vacuum chamber. Ball lenses have well-known optical properties [12,13] and are typically used for optical tweezers [14,15] but they are not traditionally used in MOTs. In our design, six collimated laser beams pass through 1.5-mm-diameter ball lenses and diverge into light cones

with a full divergence angle of approximately 35°. The conical MOT beams differ from collimated beams in that they exhibit longitudinal intensity gradients and position-dependent **k** vectors. We quantify the effects of these beam properties by measuring the key characteristics of a MOT formed at the intersection of the conical beams. In our computational analysis, we explore laser cooling in inhomogeneous highly divergent light fields and we address challenges associated with the specific geometry and beam alignment.

The ball-lens MOT design has specific advantages over the standard six-beam MOT. The trap center is enclosed in a small metal box and the ball lenses subtend a total solid angle of only a few $4\pi \times 10^{-3}$ steradians from the MOT location. Such systems can serve as an experimental platform to configure atom traps with embedded electrode structures, which may have to be mostly closed off in order to provide well-defined electromagnetic boundary conditions. Embedded electrodes with a high degree of symmetry are needed, for instance, in cold-atom-loaded Penning [16,17] and Paul traps [18]. Further, atoms trapped in a metal-box ball-lens MOT are Faraday shielded from stray electric fields and perturbations of the black-body radiation field caused by fields entering through apertures are minimized. This property can be useful in precision-measurement and atomic-clock experiments that employ MOTs and that are susceptible to black-body radiation shifts [19–22] and/or dc Stark shifts [23]. The divergence of the light cones generated by the ball lenses makes this MOT operate best at low laser powers. Because of these

*mviray@umich.edu
†eparadis@emich.edu
‡Present address: Department of Physics, Auburn University, Auburn, AL 36849, USA.

features, ball-lens atom traps can be of value in future quantum-technology applications [24].

II. IMPLEMENTATION

Six 1.5-mm-diameter N-BK7 ball lenses are held in place with a custom-made ball-lens optical box (BLOB). Figure 1(a) shows a rendering of the BLOB and Fig. 1(b) a picture of the physical part. The BLOB is a hollow cube with an inner side length of 16 mm that is manufactured from six 1.6-mm-thick steel plates. Each ball lens is implanted in a counterbore at the center of a cube face, where it is held in place by a metal flap spring, at a distance of approximately 8 mm away from the cube center and trap location. The flaps have 1.3-mm-diameter holes at the location of each lens for the MOT beams to pass through. The counterbores have inner and outer diameters of 1.3 mm and 2.0 mm, respectively. The flap springs push the lenses from the outside of the BLOB against 0.5-mm-deep ledges on the inside of the cube faces, resulting in a simple, secure, and vibration-resistant lens mount. The BLOB cube is welded onto a piece of steel square tubing that is attached to the inside of a high-vacuum (approximately 10^{-8} Torr) chamber used for MOT testing. The BLOB has eight extra 4.0-mm-diameter holes on its edges and faces as shown in Fig. 1(a), which have been added for the ease of MOT analysis and for applications requiring additional laser beams.

A sketch of the trapping fields inside the BLOB is shown in Fig. 1(c). Unlike in standard six-beam MOTs, in ball-lens MOTs the laser beams cannot be recycled by retroreflection because, due to the strong divergence of the beams in the trapping region, only a minute fraction of the trapping light is collected by the opposite ball lens [see Fig. 1(c)]. Instead, six independent collimated cooling beams (waists of $w_0 \sim 0.6$ mm) are directed onto the ball lenses from the outside of the BLOB. Inside the BLOB, the beams focus into spots at a back focal distance of approximately 350 μm and emerge as conical beams. We experimentally profile the divergent light fields inside the BLOB and determine a numerical aperture NA ≈ 0.3, corresponding to a full opening angle of the light cones of approximately 35° [full width at half maximum (FWHM) of the intensity]. The beams have an approximately Gaussian profile in the directions transverse to the beam axes, with a $1/e^2$ drop-off radius of the intensity at the MOT center of $w_B = 4$ mm. This is in agreement with a ray-tracing analysis using the Zemax OpticStudio software.

The ball-lens MOT is tested with ^{85}Rb. The MOT beams have a wavelength of 780 nm and are detuned from the $5S_{1/2}F = 3 \rightarrow 5P_{3/2}F' = 4$ hyperfine cycling transition by -14 MHz, with an uncertainty on the order of 1 MHz (F and F' denote the lower- and upper-state hyperfine quantum numbers, respectively). The power of each of the six cooling beams before entering the vacuum chamber
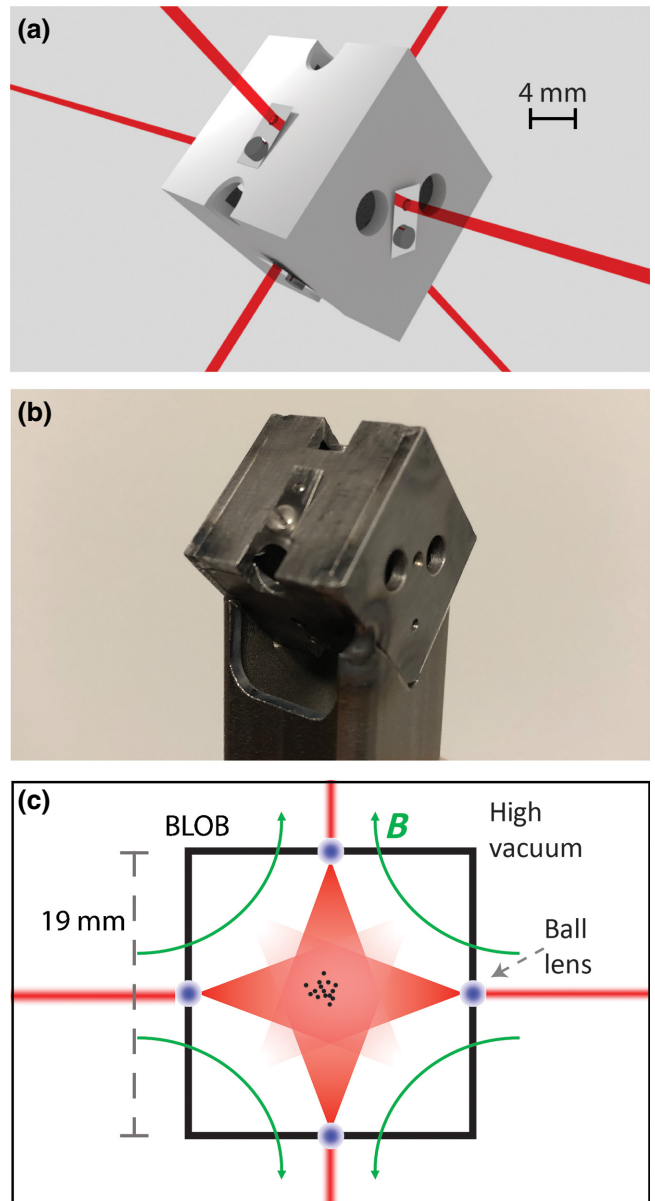

FIG. 1. (a) A computer rendering of the ball-lens MOT design, including the incident cooling beams. The ball lenses are located at the centers of the cube faces. The larger holes are for additional optical access. (b) A picture of the physical ball-lens optical box (BLOB). The right-facing side shows the exposed milled holes before insertion of a ball lens, while the upward-facing side shows an installed ball lens and retaining flap. (c) A cross-section sketch of fields within the ball-lens MOT.

is $\lesssim 5$ mW. With the above value of w_B, the upper limit of the peak intensity of the individual beams at the MOT center is approximately 12 I_{sat} (the saturation intensity $I_{\text{sat}} = 1.6$ mW/cm^2 for the MOT transition [25]). The true intensity is slightly less due to reflection and other losses (such as Rb absorption and possible beam clipping). Density images of the atom cloud in the MOT are obtained with a collimated MOT probe laser resonant with the

$F = 3 \rightarrow F' = 4$ transition (FWHM of 2.5 mm and center intensity 0.23 mW/cm²). The probe beam is directed through the center of the BLOB and the emerging output beam is aligned into a CCD camera (Pixelfly Model 270 XS). The camera is used to take both shadow images with the probe beam on and MOT beams off and fluorescence images with the probe beam off and MOT beams on. An additional camera, mounted on an axis perpendicular to that of the Pixelfly camera, is used to ensure that the trapped-atom cloud is approximately spherical. Further details of the setup are given in Appendix A.

III. MOT ANALYSIS

The main quantities of interest in our experimental characterization of the MOT are the atom number, atom density, and loading time. The atom number and density are dependent on the particular design of this MOT and the experimental laser parameters, while the loading time is mostly dependent on the background pressure in the chamber and is similar to other MOTs.

The atom number, the most important metric in our comparison with our theoretical model in Sec. IV, and the number density of the MOT are measured using shadow imaging. In this configuration, the MOT cooling beams are briefly turned off and a probe beam pulse is sent through the MOT and into the Pixelfly camera. The MOT and probe beams are switched with acousto-optic modulators (AOMs). Figure 2(a) shows an area-density shadow image for a MOT single-beam intensity of $I \approx 8.5$ mW/cm² (5.1
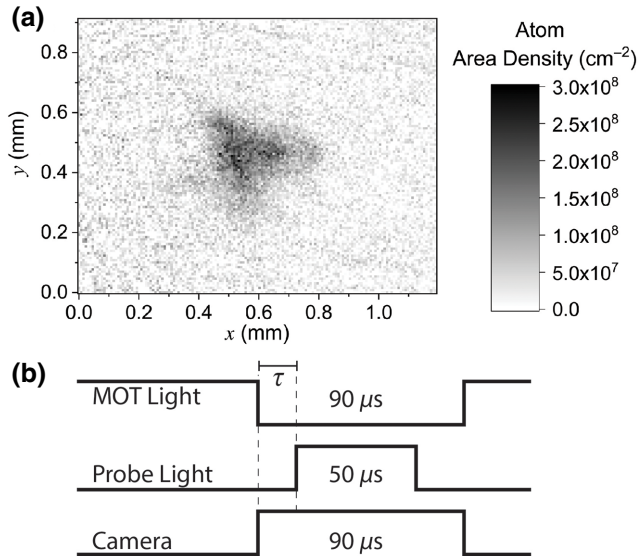

FIG. 2. (a) A shadow image of the MOT showing the area density [the integrand in Eq. (B1)] versus the position in the MOT plane. (b) The timing diagram for the shadow imaging. When the MOT light is turned off, the camera is gated on for 90 μs. Following a wait time of $\tau = 20$ μs after the MOT light is turned off, the probe pulse is turned on for a duration of 50 μs.

I_{sat}) and Fig. 2(b) shows the corresponding timing details. With the probe beam carefully tuned on resonance with the $F = 3$ to $F' = 4$ transition, we find the atom number in our MOT to be $N_{MOT,Exp} = 4.2 \times 10^5$ (for additional details, see Appendix B). Assuming that the MOT fills a cubic volume with a side length of 0.5 mm, the typical linear size of the MOT observed with both of our perpendicularly mounted cameras, the atom density in the MOT is estimated to be 3.2×10^9 atoms/cm³.

The loading time, required for calibration of the theoretical atom-number estimate in Sec. IV, is determined with fluorescence imaging. In this configuration, the MOT light is periodically switched on for 4.0 s to allow the trap to accumulate atoms and then off for 1.0 s to empty the trap. The camera records images of the atom cloud, with exposure times of 10 ms and camera-gate starting times of $\tau_i = i \times 0.25$ s relative to the turn-on of the MOT light ($i = 0, 1, \ldots, 12$). Figure 3(a) shows a fluorescence image of the atom cloud after 3.0 s of loading, along with a timing diagram in Fig. 3(b) for the fluorescence imaging procedure. In our analysis, we fit the background-subtracted fluorescence images with two-dimensional Gaussians, the pixel-sum areas of which are taken to be proportional to the atom number. The conversion factor from pixel sum to atom count is obtained as follows. A collimated 780-nm test laser test beam (power 1.134 nW) is passed in its entirety through the camera lens and is imaged into an out-of-focus nonsaturated disk with a diameter on the order of that of the MOT. The pixel sum of the test-beam image then corresponds to 1.134 nW, allowing us to convert MOT-image pixel sums into light power radiated from the MOT. The given camera geometry (lens aperture and distance from the MOT), the photon energy at 780 nm, and the photon scattering rate per atom in the MOT, $\gamma = 10^7$ s⁻¹ (known from the model results in Sec. V) then allow us to convert fluorescence into an atom count. We estimate the calibration uncertainty to be 30% due to the uncertainty in γ and in the geometrical parameters. The uncertainty in γ arises from the detuning uncertainty (a few MHz). We note that shadow imaging with a low-intensity on-resonant probe beam (see Fig. 2) results in a more accurate atom count.

Figure 3(c) presents the atom count obtained from fluorescence images versus the loading time, along with error bars from the fits that represent the statistical error (the uncertainty of the fluorescence-to-atom-count scaling is not included). Applying an exponential rise time fit to the data, we calculate a time constant of 1.3 ± 0.1 s. The residuals between the data and the fit can be attributed to the effects of intensity and frequency fluctuations of the cooling laser on the experimental data. The vacuum chamber pressure as read from the ion pump attached to the chamber is 10^{-8} Torr. The observed loading time is in line with values observed in conventional MOTs at that pressure.
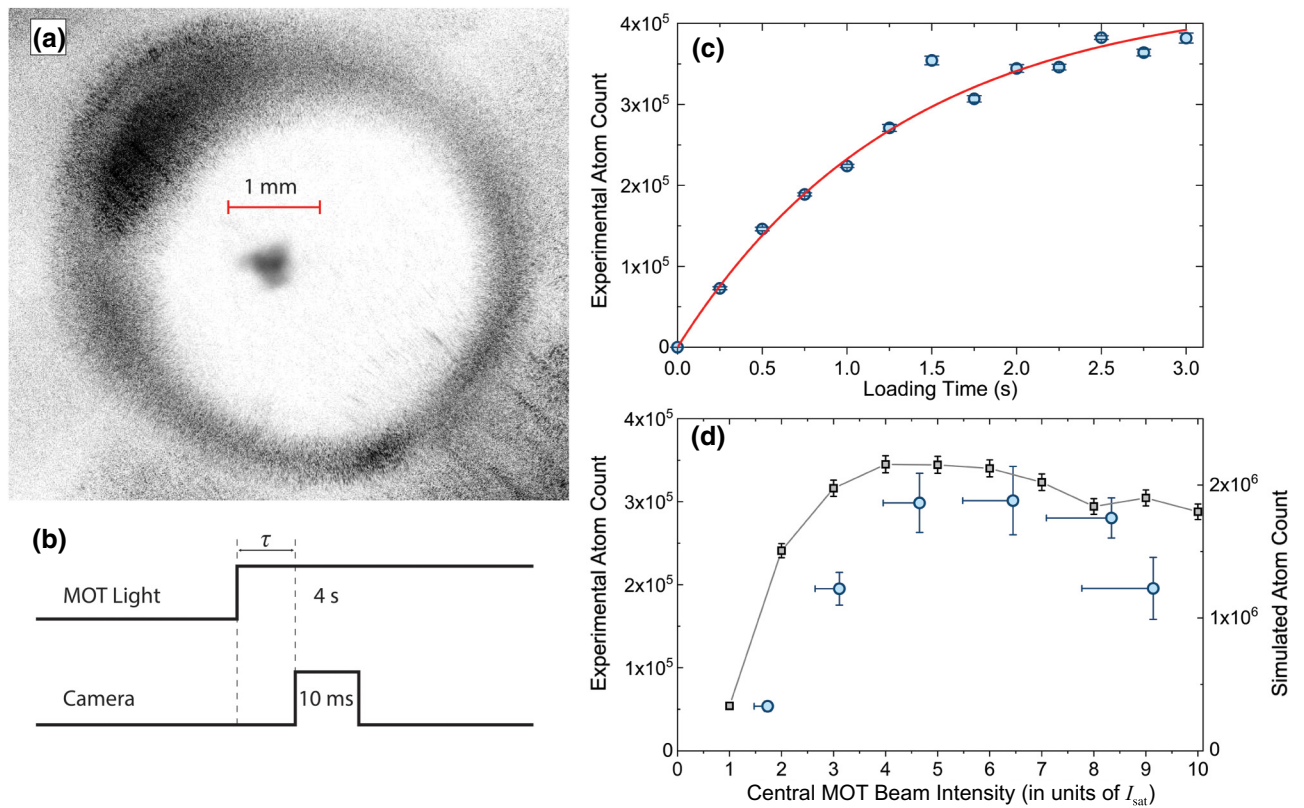
FIG. 3. (a) An inverted fluorescence image of the MOT taken through one of the 4.0-mm viewports in the BLOB, with a length scale bar. (b) The timing diagram for the loading-time measurements. The loading time τ is stepped in units of 0.25 s and the camera exposure time is 10 ms. (c) The atom count versus the loading time. The application of an exponential fit to the data yields a time constant of 1.3 ± 0.1 s. The atom count scales linearly with the trap fluorescence. (d) The measured trap atom count (left axis, circles) and the simulated trapped-atom number (right axis, linked squares) versus the central single-beam intensity at the trap center location, averaged over the six MOT beams. The asymmetric horizontal error bars reflect a potential 15% reduction of the beam intensity due to reflection and other losses, while the vertical error bars are the standard deviations of the data sets for each beam intensity. The variance in the MOT atom counts is due to shot noise as well as nonstatistical fluctuations such as radiation-pressure effects.

In our performance evaluation, we also study the dependence of the atom number on the MOT beam intensity. In Fig. 3(d), we show the atom count versus the central beam intensity. The result indicates an optimal trap performance at an intensity of approximately $6I_{sat}$; at higher intensities, the atom number drops. This behavior contrasts with standard six-beam MOTs, in which the atom number keeps increasing to considerably higher intensities before reaching a plateau. The peculiar intensity dependence of the ball-lens MOT is reproduced by our model, as shown by the simulated data in Fig. 3(d). The simulated data are for $d = 7.5$ mm, MOT detuning of -15 MHz, a MOT magnetic-field gradient of 15 Gauss/cm along the field's symmetry axis, and a MOT beam diameter of 6 mm (FWHM of the intensity). The model is described in the following sections.

IV. THEORETICAL MODEL OF BALL-LENS MOT

The objective of our model is to determine the dependence of the number of captured atoms in steady state on ball-lens MOT parameters. Further, we study how the atom-capture behavior differs from that of a standard six-beam MOT and how that translates into differences in the steady-state trapped-atom number and into guidelines for the best operating conditions for ball-lens MOTs.

Briefly, the capture efficiency is studied by simulating atom trajectories that are propagated with a fourth-order Runge-Kutta algorithm, where the six diverging ball-lens MOT beams give a spatially varying radiation pressure. In addition to the usual transverse intensity variations in the beams, we also account for the longitudinal intensity gradients and the variation of the **k** vectors within the individual highly divergent beams. We assume a fixed thermal atom flux incident from the spherical surface of the simulation volume, with random atom positions and velocities following kinetic-gas theory. Time-incremented atom positions are tracked until the atoms either exit the simulation volume or suffer a collision with a fast background atom. The trapped atoms are counted and their phase-space parameters are recorded at user-defined times. Further model details are given in Appendix C.
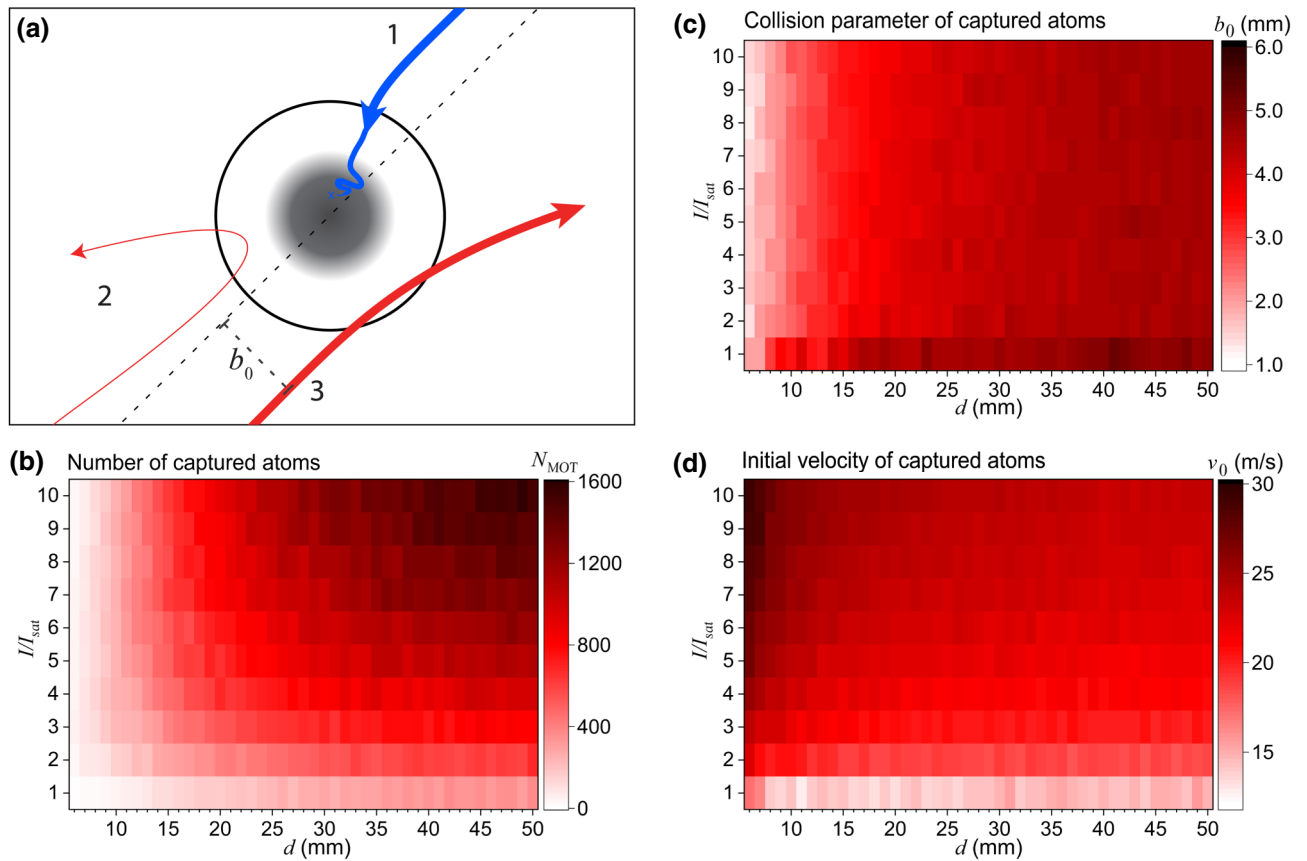
FIG. 4. (a) A depiction of three atom trajectories. The relative speeds of the atoms are indicated by the thickness of the arrows. Atom 1 is successfully trapped in the MOT. Atom 2 is not trapped because it is moving too slowly and atom 3 is not trapped because its collision parameter b_0 is too large. (b) The number of trapped atoms versus the distance d of the ball lenses from the MOT center and I/I_{sat}. (c) The root-mean-square (rms) value of the incident collision parameters b_0 of the captured atoms versus d and I/I_{sat}. (d) The rms value of the incident speed v_0 of the captured atoms versus d and I/I_{sat}.

The MOT parameters for the simulation in Fig. 4 include a MOT magnetic field gradient of 15 G/cm along the field axis and a laser detuning of -15 MHz from the MOT transition, corresponding to typical Rb MOTs and close to our experimental value. We vary the distance d of the ball-lens focal spots from the MOT center from 6 mm to 50 mm. To study the transition between a regular and the ball-lens MOT, we assume that the transverse intensity distributions of the beams are Gaussians with a *fixed, d-independent* FWHM of 6 mm at the MOT center, as measured for the ball lenses used in the experiment. The FWHMs of the beams are proportional to the distance from their respective focal spots. For large d, the system approaches a regular six-beam MOT with near-zero-NA collimated beams. As d is reduced, the MOT gradually transitions into a ball-lens MOT with large-NA beams. The smaller d is, the more the divergence and the longitudinal intensity gradient of the MOT-beam light cones affect the MOT performance. Here, we restrict ourselves to the case in which all six optical axes pass through the center of the MOT and in which all lenses have the same distance from the MOT center.

For each set of parameters, we evaluate the trajectories of 10^7–10^8 thermal atoms impinging into the MOT region. Every atom that enters gets tagged with its initial speed v_0 and collision parameter b_0 relative to the MOT center [see Fig. 4(a)]. Most atoms do not become trapped (red trajectories), while some do (blue trajectory). Any atom the speed of which drops below 1 m/s, within 2 mm from the MOT center, is considered trapped. We have verified that the exact values of these trapping criteria are not important. We log the root-mean-square (rms) velocity and rms radius of the trapped-atom cloud in the MOT, the trapped-atom number, the average photon scattering rate of the atoms, and the rms values of the initial speed v_0 and the collision parameter b_0 of the atoms that become trapped.

V. RESULTS OF THEORETICAL MODEL

A. Survey of relative performance

In Fig. 4, we present a survey of ball-lens MOT performance as a function of the ball-lens-to-focal-spot distance d and the single-beam peak intensity I at the MOT center.

In the simulation, the MOT loads for 0.9 s, the half-life for the collision time constant of 1.3 s measured in the experiment. The simulated impingement flux into the MOT cell, F_{Sim}, is taken to be 50 atoms per microsecond [the trapping results can be scaled up to the actual impingement flux; see Eq. (1) below]. Figure 4(a) shows a diagram of typical atom trajectories in the MOT, two of which fail while one is successful in becoming trapped. Figure 4(b) displays the number of captured atoms N_{MOT} versus d and I/I_{Sat}. From this simulation, it is determined that in the experiment we are operating the MOT near the lower bound in d at which the ball-lens MOT becomes viable. At $d \lesssim 7$ mm, the ball-lens MOT does not capture experimentally useful numbers of atoms. The usual six-beam MOT with collimated beams is near equivalent with the right margins in Figs. 4(b)–4(d), where $d = 50$ mm. The numerical data show that, at -15 MHz MOT detuning and other parameters as stated, our $d \approx 8$ mm ball-lens MOT captures approximately 6%–14% of the number of atoms that one would find in a regular six-beam MOT, with the highest ratio at $I = 4I_{\text{Sat}}$. It is also noted that at small d values the performance is best at lower intensities and degrades at high intensities. This accords with the trend measured in Fig. 3(d). For completeness, we also report that the temperature of the trapped atoms is, universally for all cases in Fig. 4, near the Doppler limit (here, 150 μK), and the diameter of the trapped-atom cloud near 0.25 mm.

In Fig. 4(c), it is seen that the rms incident collision parameter b_0 of the trapped atoms drops from about 5 mm for the regular MOT ($d = 50$ mm) to about 1.5 mm for the case of extremely divergent beams ($d = 6$ mm), with a minor variation as a function of the intensity. Figure 4(d) shows that for the standard MOT ($d = 50$ mm) the rms capture velocity ranges between 15 m/s at low and 25 m/s at high intensity; this range is generally as expected. Interestingly, for extremely divergent beams ($d \lesssim 8$ mm), the rms capture velocities increase to about 17 m/s at low and 30 m/s at high intensity. A closer study, shown in Appendix D, reveals that MOTs with extremely divergent beams do not capture significant fractions of slow incident atoms at all. This behavior may appear counterintuitive, but we offer an explanation for this in the discussion and in Appendix D.

B. Quantitative model for the number of trapped atoms

Next, we perform an order-of-magnitude comparison between experimentally observed and simulated trapped-atom numbers. The Rb vapor pressure inside the BLOB is assumed to be negligible; the atoms to be trapped impinge from the larger vacuum chamber ("outer vacuum chamber") via the apertures into the interior of the BLOB. The atom flux impinging from the outer vacuum chamber into the BLOB cell is given by $F_{\text{Exp}} = (A/4)n_V \bar{v}$, where A is the surface area of the cell that is exposed to impinging thermal atoms, n_V is the vapor volume density in the outer vacuum chamber, and $\bar{v} = \sqrt{8k_B T/(\pi M)}$ with vapor temperature $T = 293$ K and atom mass $M = 85$ amu is the average thermal speed. It is invalid to set n_V equal to the room-temperature equilibrium density of Rb, because the outer vacuum chamber is not saturated with Rb vapor. For a good comparison, it is essential to perform an *in situ* reference absorption measurement, from which n_V is inferred. For the necessary calibration of n_V, we perform a reference absorption measurement with a Gaussian-profile test-beam diameter < 1 mm (central intensity 11 mW/cm^2, tuned to the MOT transition) propagating through a 40-cm-long segment of the outer vacuum chamber, with the MOT magnetic field off. The observed absorption is $3.6 \pm 0.2\%$. Using a calculation described in Appendix E, we find $n_V = 6.3 \times 10^{13}$ m^{-3}, which yields an experimental impingement flux $F_{\text{Exp}} = A\bar{v}n_V/4 = 4.3 \times 10^{11}$ s^{-1}.

In the simulation, the impingement flux into the MOT cell is assumed to be $F_{\text{Sim}} = 5 \times 10^7$ s^{-1}. Therefore, if the simulation shows a trapped-atom number $N_{\text{MOT,Sim}}$, the number of trapped atoms expected for our experiment is

$$N_{\text{MOT,Exp}} = N_{\text{MOT,Sim}} \frac{F_{\text{Exp}}}{F_{\text{Sim}}} = 8600 N_{\text{MOT,Sim}}. \quad (1)$$

We run the simulation for a best estimate of our experimental conditions ($d = 7.5$ mm, beam FWHM of 6 mm, MOT decay time of 1.3 s, magnetic-field gradient along the field axis 15 G/cm). Over the parameter ranges and step sizes investigated in our simulations, the best performance is seen for a MOT detuning of about -15 MHz and $I = 6I_{\text{sat}}$. Under these conditions, the simulated steady-state atom number is 220 ± 4. The theoretically predicted value for the trapped atom number then becomes $N_{\text{MOT,Sim}} = 1.9 \times 10^6$. This number can be compared with the number of MOT atoms that we have experimentally observed under good conditions, $N_{\text{MOT,Exp}} = 4.2 \times 10^5$.

VI. DISCUSSION

The picture that emerges from the combined results of the survey study is that ball-lens MOTs with highly divergent trapping beams ($d \lesssim 8$ mm, NA $\gtrsim 0.3$) only capture atoms that are pointing toward an "active" trapping center that is about 4 mm across [the gray region in Fig. 4(a)]. Atoms traversing through an outer belt of radiation pressure, ranging in diameter from about 4 mm to the outer reaches of the trapping beams, become blown out on their approach toward the MOT center [trajectory 3 in Fig. 4(a)]. Ball-lens MOTs with highly divergent trapping beams therefore only capture atoms with velocities between 20 m/s and 30 m/s and collision parameters less than about 2 mm. It is particularly noteworthy that atoms slower than about 15 m/s and with collision parameters less than about 2 mm do not become trapped [trajectory

2 in Fig. 4(a)]. For an atom to become trapped, it has to be fast enough that its inertia carries it through the outer belt of radiation pressure, slow enough that it becomes trapped within the inner region of "good" radiation pressure, and the trajectory of the incident atom also has to point at the center of the MOT to within about 2 mm tolerance. In Fig. 4(a), only trajectory 1 meets all criteria. Additional details presented in Appendix D confirm this picture.

The agreement between experimental and simulated trapped-atom numbers is within about a factor of 4. Four of the eight 4-mm holes on the BLOB have a small clearance from the glass windows, which are part of the outer vacuum chamber, and one window is hidden in the BLOB's support tube. The accessible opening of the BLOB where Rb may effuse is only $3/8 = 1/2.7$ of the area assumed in comparison, leaving a disagreement in trapped-atom number of less than a factor of two. The remaining disagreement may, in part, be attributed to Rb vapor-density variations near the BLOB, caused by the complex molecular-streaming behavior of the Rb vapor from the source, which is attached to the outer vacuum chamber, to the BLOB region. The ball-lens MOT's atom collection efficiency could also be reduced by MOT beam aberrations and imperfections that we are not able to quantify but that are usually present in most MOT setups. Finally, there may be a small difference between the assumed $J = 0 \rightarrow J' = 1$ MOT transition and the actual ^{85}Rb $F = 3 \rightarrow F' = 4$ transition in terms of trapping efficiency. Studies into the detailed origins of the remaining factor of 2 of unaccounted-for disagreement are outside the scope of the present study. Regardless, we are confident that we capture the essential physical principles of the ball-lens MOT and that our work presents a valuable guide for research elsewhere toward implementation of this design.

VII. CONCLUSION

We implement a magneto-optical trap within a small metallic cube using 1.5-mm-diameter ball lenses and we develop a kinetic model that describes atom trapping and cooling in MOTs with highly divergent trapping beams. The simulated results are in good agreement with our experimental observations and parametrize the range over which this MOT should work well.

While this design of the BLOB is successful in forming a MOT, there are several changes that we will implement for subsequent versions. The simulations indicate that our ball-lens-to-focal-spot distance d from the trap center is near the lower edge of viability. In view of Fig. 4, in applications one might want to use d values in the range of 2 cm, where the BLOB dimension is still conveniently small and the atom number is $\gtrsim 50\%$ of that of a similar-sized standard six-beam MOT.

We will be remiss if we do not mention the disadvantages of this MOT design. Unlike standard designs, it is difficult to counter-align the beams that lie along the same axis, making the initial alignment more difficult. Due to the dependence of the central intensity in the MOT region on the incident angle on the ball lens, the setup has a higher sensitivity to relative beam powers than a standard MOT. Nevertheless, once we observe trapped atoms within the ball-lens MOT, the design provides a sizable range of stability over both the relative beam powers and angles of incidence for each ball lens.

Now that the viability of a ball-lens MOT is demonstrated, the design may be applied in experiments. The compact BLOB provides well-defined electrostatic boundary conditions and provides a platform to install additional electrodes. This feature makes the BLOB design attractive for research on cold plasmas generated from trapped-atom clouds, where uncontrolled dc electric fields can be a problem. Further, other groups have recently performed work on compact ion traps and trapped-ion laser cooling [26–28]. The advantages of the ball-lens MOT would coincide well with some requirements of these types of experiments. The well-defined electrostatic boundary conditions minimize stray electric fields inside the trapping region and eliminate dc Stark effects [23]. A BLOB enclosure with six isolated walls connected to electrodes would afford full three-dimensional electric field control. This type of BLOB architecture could allow stray-electric-field control in precision spectroscopy experiments with dipole traps [29] and single ion traps [30]. As another example, cylindrically symmetric implementations of BLOBs, with segmented electrode rings and disks, would be compatible with the symmetry requirements of Penning traps [31].

We note that the velocity range of cold-atomic-beam sources, such Zeeman slowers and LVISs [32,33] with an optional pusher beam, can be matched with the velocity capture range of the ball-lens MOT, which ranges from 20 m/s to 30 m/s. A matched-velocity configuration would allow for more efficient loading of a ball-lens MOT.

Finally, the BLOB also provides an effective shield against radio-frequency, thermal, and optical radiation entering the box, because the solid angle subtended by the ball lenses from the center of the box can be made less than one thousandth of 4π and the hole sizes for the ball lenses are only about 1 mm in diameter. A BLOB design may therefore aid in controlling ac Stark and ponderomotive shifts in high-precision spectroscopy work with Rydberg atoms [34,35]. It may also help in addressing ac Stark shifts induced by black-body radiation [19–22] and dc Stark shifts [23] in optical-lattice optical clocks. In some of these applications, it will be necessary to eliminate the unused 4-mm apertures we have implemented for flexibility in diagnostic tests of our MOT or to replace them with pinholes, so as to not compromise the integrity of the electromagnetic boundary with large apertures.

APPENDIX A: EXPERIMENTAL DETAILS

The BLOB is tightly mounted between two large-diameter re-entrant vacuum windows that are part of a larger outer vacuum chamber that houses the BLOB. The two MOT coils are placed close to the outsides of the re-entrant windows, so that the separation between the inner-most windings of the coil pair is approximately 40 mm. The MOT coils run at a current of approximately 6 A and are air convection cooled. The experiment is equipped with bias field coils to adjust the zero position of the MOT quadrupole field.

The MOT cooling laser is locked to a hyperfine component of the $5S_{1/2} \rightarrow 5P_{3/2}$ transition of ^{85}Rb using saturation spectroscopy in a Rb vapor cell [36]. The cooling beam passes through an AOM for switching and for frequency tuning close to the $F = 3 \rightarrow F' = 4$ hyperfine transition. A repumper laser drives the $F = 2 \rightarrow F' = 3$ hyperfine transition. The power of each cooling beam before entering the vacuum chamber is $\lesssim 5$ mW. The setup also has a probe laser used for shadow imaging. This laser is on resonance with the $F = 3 \rightarrow F' = 4$ hyperfine transition and also passes through an AOM for frequency tuning and for switching.

APPENDIX B: SHADOW IMAGING

The value for the atom number in the MOT, $N_{\text{MOT,Exp}}$, is found by evaluating

$$N_{\text{MOT,Exp}} = \int \frac{1}{\sigma} \ln\left(\frac{I_0(x,y) - I_B(x,y)}{I(x,y) - I_B(x,y)}\right) dx\,dy \quad \text{(B1)}$$

over the MOT object plane, where $I(x,y)$ is the shadow image with MOT atoms present, $I_B(x,y)$ is a background image with the probe beam off but all other light sources left on, and $I_0(x,y)$ is an image with the probe beam on but without MOT atoms. Since the light is unpolarized and the MOT magnetic field is left on, we use the isotropic absorption cross section $\sigma = 1.246 \times 10^{-9}$ cm^2 [25]. The integral is evaluated as a discrete sum over a two-dimensional array of CCD pixels, with the pixel area given by the CCD pixel area projected into the object (MOT) plane.

APPENDIX C: MODEL DETAILS

In our kinetic laser-cooling model, we assume a spherical MOT cell volume of radius $R = 1.0$ cm, which has a volume similar to that of the BLOB used in the experiment. Thermal atoms are generated at a fixed rate F_{Sim} on the cell surface with fixed radial coordinate R and random polar

and azimuthal angles (θ_0, ϕ_0), with the coordinate system defined by the magnetic field symmetry axis ($\hat{\mathbf{z}}$) and the axes of the cooling beams. The inward velocity distribution is known from gas kinetics:

$$P(v, \theta, \phi) = \frac{1}{\pi} P(v) \sin(\theta) \cos(\theta), \quad \text{(C1)}$$

with a normalized effusive Maxwell distribution $P(v)$ and spherical angular coordinates relative to the normal of the impingement surface [which depends on the position angles (θ_0, ϕ_0) of the atom]. The atomic trajectories are propagated with a fourth-order Runge-Kutta routine in which the atoms are subjected to the net radiation pressure force from the six MOT beams. The actual position $\mathbf{r}(t)$ of an atom determines the position-dependent beam intensities, the beam $\mathbf{k}$ vectors, and the local MOT magnetic field. Due to the conical nature of the light fields, the $\mathbf{k}$ vectors of a given beam depend on the position within the beam and cover an angular range that depends on the NA. Along the optical axis of a beam, the transverse FWHM increases linearly with distance from the ball lens and the intensity decreases quadratically with distance. Further, the polarization of each beam is locally decomposed into three polarization components (linear, left-handed circular, and right-handed circular) relative to the local direction of the magnetic field. Hence, the six MOT beams together give rise to 18 radiation-pressure force components acting on the atom, where each component has the described dependencies on position. Saturation of the assumed $J = 0$ to $J' = 1$ MOT transition (wavelength 780 nm, saturation intensity 1.6 mW/cm^2, upper-state decay rate $2\pi \times 6$ MHz) is taken into account. To account for spontaneous emission of the atoms on the laser-cooling transition, the program implements photon-recoil kicks in random directions, chosen with random numbers. Further, every atom carries a lifetime clock that measures the time elapsed after entry of the atom into the simulation. The time elapsed governs the exponential decay of the atom. Physically, an atom decay is a collision of a MOT atom with a fast background gas atom. A collision effectively removes the atom from the simulation. Atom decays are implemented using random numbers. The $1/e$ atom decay time is chosen to be 1.3 s, the value observed in our experiment.

APPENDIX D: TRAPPING STATISTICS IN MOTs WITH HIGHLY DIVERGENT CONICAL BEAMS

To further exhibit the trapping behavior in MOTs with highly divergent beams, we perform a study in which both the collision parameter, b_0, and the incident velocity, v_0, are kept fixed, while the polar and azimuthal angles of approach of the incident atoms relative to the z-axis, θ_{inc} and ϕ_{inc}, are chosen at random. The results shown in Fig. 5 demonstrate that in the MOT with highly divergent laser beams, atoms with incident velocities $v_0 \lesssim 18$ m/s become
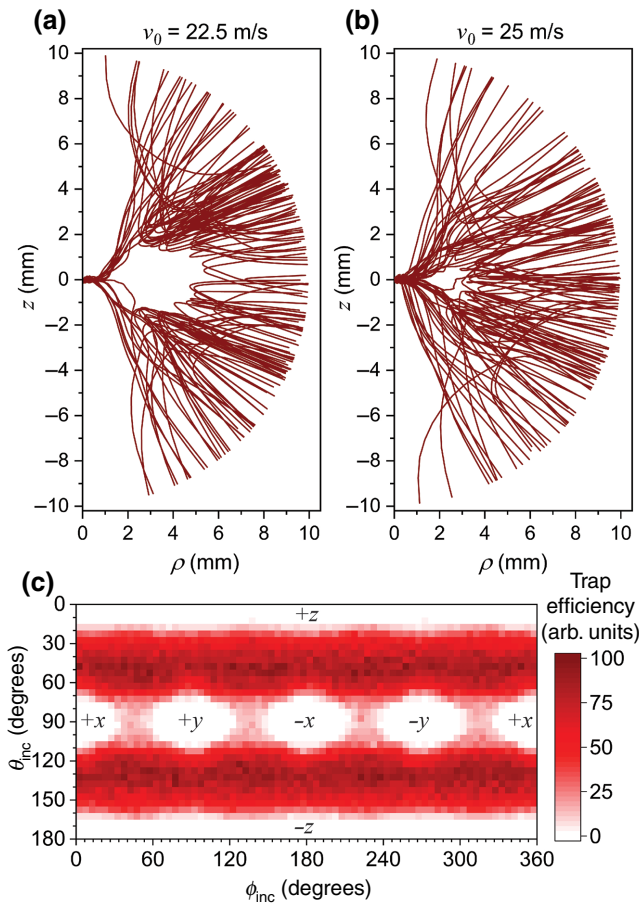
FIG. 5. (a),(b) Trajectory samples in cylindrical coordinates for $I = 6I_{sat}$, $d = 7$ mm, $b_0 = 1$ mm, MOT detuning of -15 MHz, and initial speeds of $v_0 = 22.5$ m/s and $v_0 = 25.0$ m/s, respectively. Many trajectories that are strongly curved are associated with repulsion by radiation pressure, while trajectories that are approximately straight and end at the origin show trapping events. (c) The statistics of the trapped-atom counts versus the polar and azimuthal angles of approach, θ_{inc} and ϕ_{inc}, of the incident atoms, for the same parameters as in (b) and on a linear scale. The angular regions of no trapping (white) correspond with the directions of the MOT laser beams, indicated by the coordinate-axis labels.

repelled and are not trapped due to radiation pressure. Atoms that do become trapped have velocities $v_0 \sim 25$ m/s and collision parameters $b_0 \lesssim 2$ mm. The trapping behavior as a function of the angle of approach of the impinging atoms, θ_{inc} and ϕ_{inc}, displayed in Fig. 5(c), further shows that atoms approaching from directions that are in between the MOT laser-beam directions have a much higher chance for trapping than atoms approaching from a direction that is close to one of the MOT-beam directions [see the beam labels in Fig. 5(c)].

The above-described features differ starkly from the case of a regular MOT, in which practically all atoms with $v_0 \lesssim 30$ m/s and $b_0 \lesssim 6$ mm are collected. The contrast in trapping behavior of MOTs with highly divergent and
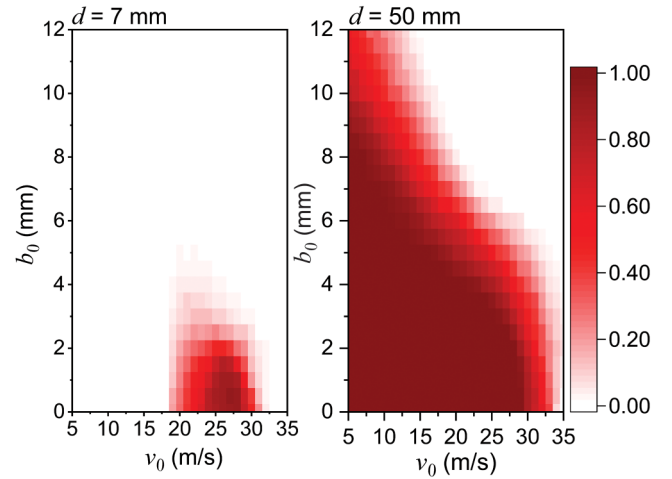

FIG. 6. The probability of trapping on the indicated linear scale averaged over θ_{inc} and ϕ_{inc} versus the incident atom velocity v_0 and collision parameter b_0 for a highly divergent ball-lens MOT with $d = 7$ mm (left) and for an essentially regular MOT with $d = 50$ mm (right).

regular MOTs with collimated beams is shown quantitatively in Fig. 6, where we display the relative capture efficiencies versus b_0 and v_0 for the cases $d = 7$ mm (MOT with highly divergent beams) and $d = 50$ mm (near-ideal regular MOT). While both MOTs are capturing atoms up to about 30 m/s, the MOT with highly divergent beams fails to capture slow atoms and atoms with collision parameters larger than about 2 mm. This behavior is due to repulsive radiation pressure at distances larger than about 2 mm (see Fig. 5).

APPENDIX E: VAPOR DENSITY CALIBRATION

To calibrate the Rb vapor density in the outer vacuum chamber that houses the BLOB, we apply a numerical absorption model in which we assume a thermal Rb vapor with a Maxwell velocity distribution for 293 K and an unknown volume density n_V. In the model, the Gaussian probe beam is segmented into annular rings with given intensities, radii, and radial step sizes. The velocity-averaged absorption coefficient, which depends on intensity due to saturation of the transition, is calculated for each ring. There, we use the intensity measured at the probe-beam center of 2.8 $I_{sat,i}$, with the isotropic saturation intensity $I_{sat,i} = 3.9$ mW/cm^2, and the isotropic on-resonance absorption cross section $\sigma = 1.246 \times 10^{-9}$ cm^2 [25]. The beam power transmitted through the 40-cm-long beam path through the outer vacuum chamber is then found by integration over the annular rings. The calculation yields the beam-power absorption percentage as a function of the atom volume density, n_V. We find that the experimentally observed $(3.6 \pm 0.2)\%$ power loss requires $n_V = 6.3 \times 10^{13}$ m^{-3}, with a 6% relative uncertainty.

With the average thermal speed of $\bar{v} = 270$ m/s, the impingement flux density then follows as $\bar{v}n_V/4 = 4.3 \times 10^{15}$ m^{-2} s^{-1}. Multiplication of this value with the cross-section area A of all apertures leading into the BLOB (eight 4-mm-diameter holes in our experiment) then yields an experimental impingement flux $F_{\mathrm{Exp}} = A\bar{v}n_V/4 = 4.3 \times 10^{11}$ s^{-1}.

It is noted that the measured value of n_V represents an average over the length of the probe beam and that the uncertainty of the local n_V value at the location of the BLOB access holes may be greater than that of the beam-averaged n_V. Based on visual observation of the fluorescence glow along the probe beam path with an infrared viewer, we see no evidence for density variations. Nevertheless, Rb adsorption on the BLOB metal walls, in close proximity to the BLOB access holes, could locally reduce the atom density in a way that is hard to see.

---

[1] E. Raab, M. Prentiss, A. Cable, S. Chu, and D. Pritchard, Trapping of Neutral Sodium Atoms with Radiation Pressure, Phys. Rev. Lett. **59**, 2631 (1987).

[2] H. J. Metcalf and P. van der Straten, *Laser Cooling and Trapping* (Springer, New York, 1999).

[3] W. D. Phillips, Nobel lecture: Laser cooling and trapping of neutral atoms, Rev. Mod. Phys. **70**, 721 (1998).

[4] J. Lee, J. A. Grover, L. A. Orozco, and S. L. Rolston, Sub-Doppler cooling of neutral atoms in a grating magneto-optical trap, J. Opt. Soc. Am. B **30**, 2869 (2013).

[5] E. Imhof, B. K. Stuhl, B. Kasch, B. Kroese, S. E. Olson, and M. B. Squires, Two-dimensional grating magneto-optical trap, Phys. Rev. A **96**, 033636 (2017).

[6] K. Lee, J. Kim, H. Noh, and W. Jhe, Single-beam atom trap in a pyramidal and conical hollow mirror, Opt. Lett. **21**, 1177 (1996).

[7] J. Arlt, O. Marago, S. Webster, S. Hopkins, and C. Foot, A pyramidal magneto-optical trap as a source of slow atoms, Opt. Commun. **157**, 303 (1998).

[8] M. Vangeleyn, P. F. Griffin, E. Riis, and A. S. Arnold, Single-laser, one beam, tetrahedral magneto-optical trap, Opt. Express **17**, 13601 (2009).

[9] A. Hinton, M. Perea-Ortiz, J. Winch, J. Briggs, S. Freer, D. Moustoukas, S. Powell-Gill, C. Squire, A. Lamb, C. Rammeloo *et al.*, A portable magneto-optical trap with prospects for atom interferometry in civil engineering, Philos. Trans. R. Soc. London, Ser. A **375**, 20160238 (2016).

[10] Z. Lu, K. Corwin, M. Renn, M. Anderson, E. Cornell, and C. Wieman, Low-Velocity Intense Source of Atoms from a Magneto-Optical Trap, Phys. Rev. Lett. **77**, 3331 (1996).

[11] A. di Stefano, D. Wilkowski, J. Müller, and E. Arimondo, Five-beam magneto-optical trap and optical molasses, Appl. Phys. B **69**, 263 (1999).

[12] Edmund Optics Worldwide, Understanding ball lenses, https://www.edmundoptics.com/knowledge-center/application-notes/optics/understanding-ball-lenses/ (2020).

[13] M.-S. Kim, T. Scharf, S. Mühlig, M. Fruhnert, C. Rockstuhl, R. Bitterli, W. Noell, R. Voelkel, and H. P. Herzig,
Refraction limit of miniaturized optical systems: A ball-lens example, Opt. Express **24**, 6996 (2016).

[14] M. Sasaki, T. Kurosawa, and K. Hane, Micro-objective manipulated with optical tweezers, Appl. Phys. Lett. **70**, 785 (1997).

[15] T. Numata, A. Takayanagi, Y. Otani, and N. Umeda, Manipulation of metal nanoparticles using fiber-optic laser tweezers with a microspherical focusing lens, Jpn. J. Appl. Phys. **45**, 359 (2006).

[16] G. Gabrielse, P. Larochelle, D. Le Sage, B. Levitt, W. S. Kolthammer, R. McConnell, P. Richerme, J. Wrubel, A. Speck, and M. C. George *et al.* (ATRAP Collaboration), Antihydrogen Production within a Penning-Ioffe Trap, Phys. Rev. Lett. **100**, 113001 (2008).

[17] J.-H. Choi, B. Knuffman, X. H. Zhang, A. P. Povilus, and G. Raithel, Trapping and Evolution Dynamics of Ultracold Two-Component Plasmas, Phys. Rev. Lett. **100**, 175002 (2008).

[18] S. Schmid, A. Härter, A. Frisch, S. Hoinka, and J. H. Denschlag, An apparatus for immersing trapped ions into an ultracold gas of neutral atoms, Rev. Sci. Instrum. **83**, 053108 (2012).

[19] A. Golovizin, E. Fedorova, D. Tregubov, D. Sukachev, K. Khabarova, V. Sorokin, and N. Kolachevsky, Inner-shell clock transition in atomic thulium with a small blackbody radiation shift, Nat. Commun. **10**, 1724 (2019).

[20] Y.-L. Xu and X.-Y. Xu, Analysis of the blackbody-radiation shift in an ytterbium optical lattice clock, Chin. Phys. B **25**, 103202 (2016).

[21] I. Ushijima, M. Takamoto, M. Das, T. Ohkubo, and H. Katori, Cryogenic optical lattice clocks, Nat. Photonics **9**, 185 (2015).

[22] V. V. Flambaum, S. G. Porsev, and M. S. Safronova, Energy shift due to anisotropic blackbody radiation, Phys. Rev. A **93**, 022508 (2016).

[23] K. Beloy, X. Zhang, W. F. McGrew, N. Hinkley, T. H. Yoon, D. Nicolodi, R. J. Fasano, S. A. Schäffer, R. C. Brown, and A. D. Ludlow, Faraday-Shielded dc Stark-Shift-Free Optical Lattice Clock, Phys. Rev. Lett. **120**, 183201 (2018).

[24] V. I. Yudin, A. V. Taichenachev, M. V. Okhapkin, S. N. Bagayev, C. Tamm, E. Peik, N. Huntemann, T. E. Mehlstäubler, and F. Riehle, Atomic Clocks with Suppressed Blackbody Radiation Shift, Phys. Rev. Lett. **107**, 030801 (2011).

[25] D. A. Steck, Rubidium 85 D line data, Available online at http://steck. us/alkalidata (Revision 2.1.6, 20 September 2013).

[26] B. J. McMahon, C. Volin, W. G. Rellergert, and B. C. Sawyer, Doppler-cooled ions in a compact reconfigurable Penning trap, Phys. Rev. A **101**, 013408 (2020).

[27] Z. Andelkovic, R. Cazan, W. Nörtershäuser, S. Bharadia, D. M. Segal, R. C. Thompson, R. Jöhren, J. Vollbrecht, V. Hannen, and M. Vogel, Laser cooling of externally produced Mg ions in a Penning trap for sympathetic cooling of highly charged ions, Phys. Rev. A **87**, 033423 (2013).

[28] J. F. Goodwin, G. Stutter, R. C. Thompson, and D. M. Segal, Resolved-Sideband Laser Cooling in a Penning Trap, Phys. Rev. Lett. **116**, 143002 (2016).

[29] R. J. Rengelink, Y. van der Werf, R. P. M. J. W. Notermans, R. Jannin, K. S. E. Eikema, M. D. Hoogerland,

and W. Vassen, Precision spectroscopy of helium in a magic wavelength optical dipole trap, Nat. Phys. **14**, 1132 (2018).

[30] P. B. R. Nisbet-Jones, S. A. King, J. M. Jones, R. M. Godun, C. F. A. Baynham, K. Bongs, M. Doležal, P. Balling, and P. Gill, A single-ion trap with minimized ion-environment interactions, Appl. Phys. B **122**, 57 (2016).

[31] T. M. Squires, P. Yesley, and G. Gabrielse, Stability of a Charged Particle in a Combined Penning-Ioffe Trap, Phys. Rev. Lett. **86**, 5266 (2001).

[32] Z. Lu, K. Corwin, M. Renn, M. Anderson, E. A. Cornell, and C. Wieman, Low-Velocity Intense Source of Atoms from a Magneto-Optical Trap, Phys. Rev. Lett. **77**, 3331 (1996).

[33] C. Y. Park, M. S. Jun, and D. Cho, Magneto-optical trap loaded from a low-velocity intense source, JOSA B **16**, 994 (1999).

[34] J. W. Farley and W. H. Wing, Accurate calculation of dynamic Stark shifts and depopulation rates of Rydberg energy levels induced by blackbody radiation. Hydrogen, helium, and alkali-metal atoms, Phys. Rev. A **23**, 2397 (1981).

[35] A. Ramos, K. Moore, and G. Raithel, Measuring the Rydberg constant using circular Rydberg atoms in an intensity-modulated optical lattice, Phys. Rev. A **96**, 032513 (2017).

[36] W. Demtröder, *Laser Spectroscopy* (Springer, Berlin Heidelberg, 2008).